UNIVERSITY OF CALIFORNIA,
IRVINE

Rydberg exciton states and near-infrared light-emitting diode in monolayer $MoTe_2$ devices

THESIS

submitted in partial satisfaction of the requirements
for the degree of

MASTER OF SCIENCE

in Physics

by

Sebastian Yepez Rodriguez

Thesis Committee:
Assistant Professor Luis A. Jauregui, Chair
Professor Ilya N. Krivorotov
Assistant Professor Javier D. Sanchez-Yamagishi

2024

Table of Contents

List of Symbols

TMDs	Transition metal dichalcogenides
2D	Two-dimensional
$MoTe_2$	Molybdenum ditelluride
NIR	Near-infrared
SOC	Spin-orbit coupling
Δ_c	Conduction band splitting
$\Delta_{Dark-Bright}$	Dark-bright exciton energy difference
E_n	Exciton emission energy
E_g	Free-particle bandgap energy
$E_{b(n)}$	Binding energy of Rydberg exciton state
n	Principal quantum number of Rydberg state
$\hbar$	Planck's constant
μ	Exciton reduced mass
r_n	Exciton effective Bohr radius
PL	Photoluminescence
EL	Electroluminescence
AC	Alternating current
A_{1g}	Out-of-plane mode of $MoTe_2$ at ~170 cm^{-1}
E^1_{2g}	In-plane mode of $MoTe_2$ at ~235 cm^{-1}
B_{2g}	Out-of-plane mode of $MoTe_2$ at ~290 cm^{-1}
λ	Wavelength
NA	Numerical aperture
CCD	Charge-coupled device
RT	Room temperature
SEM	Scanning electron microscopy
BN	Boron nitride
SiO_2	Silicon dioxide

PDMS	Polydimethylsiloxane
PC	Polycarbonate
EBL	Electron beam lithography
MMA	Methyl methacrylate
PMMA	Poly(methyl methacrylate)
X_{1s}^{0}	Ground state neutral exciton
X_{1s}^{T}	Ground state charged exciton
$X_{1s}^{T,1}$	Lower energy charged exciton
$X_{1s}^{T,2}$	Higher energy charged exciton
X_{2s}^{0}	First excited state neutral exciton
X_{2s}^{T}	First excited state charged exciton
V_G	Gate voltage
CNP	Charge neutrality point
FFT	Fast Fourier transform
I_{PL}	Integrated PL intensity
I_{EL}	Integrated EL intensity
C	Proportionality constant
κ	Constant that allows fitting of data
P	Power
α	Coefficient indicating the excitonic species
I_i	Lorentzian function
A_i	Amplitude of Lorentzian
E_i	Emission energy of excitonic species
Γ_i	Linewidth of Lorentzian
V_{DS}	Drain-source voltage
I_{DS}	Drain-source current
LED	Light-emitting diode
R	Resistance

List of Figures

Acknowledgments

First of all, I would like to express my deepest gratitude to my advisor and committee chair, Dr. Luis A. Jauregui, for his continuous support in research and for having the patience to bear with me until the end. I will always be grateful to him for having taken me as an intern in 2020, and then as a graduate student. Without his guidance and help, this thesis would not have been possible.

I would like to thank my committee members, Dr. Ilya Krivorotov and Dr. Javier Sanchez-Yamagishi, for taking the time to review this thesis, and for helping me along the way to be a better person.

This thesis could not have been done without the work performed by Dr. Jinyu Liu on the crystal growth of bulk semiconducting samples, Marshall Campbell on the Raman measurements and help using the PL setup, and Triet Ho on the rendering of 3D images. I am very grateful to them.

This research was primarily supported by the National Science Foundation NSF-CAREER (DMR 2146567), and was partially supported by the National Science Foundation Materials Research Science and Engineering Center program through the UC Irvine Center for Complex and Active Materials (DMR-2011967).

Abstract of the Thesis

Rydberg exciton states and near-infrared light-emitting diode in monolayer $MoTe_2$ devices

by

Sebastian Yepez Rodriguez

Master of Science in Physics

University of California, Irvine, 2024

Assistant Professor Luis A. Jauregui, Chair

Excitons, or bound electron-hole pairs, play a crucial role in the optical response of monolayer, 2H-phase transition-metal dichalcogenides (TMDs). They hold significant promise for the development of novel quantum opto-electronic devices due to their large binding energies and strong spin-orbit coupling. Among the monolayer TMDs, $MoTe_2$ stands out because of its bandgap in the near-infrared (NIR) regime. Here, we report the experimental observation of NIR Rydberg excitons and conduction band-split charged excitons, in high-quality, boron nitride (BN)-encapsulated monolayer $MoTe_2$ devices, probed by photoluminescence and electroluminescence spectroscopy. By employing a graphite bottom gate, we successfully modulate the emission intensity of various excitonic species. Additionally, our device fabrication process within an argon-filled glove box ensures clean TMD/metal electrode interfaces, enabling the construction of p-n junctions near the electrodes. Our work significantly advances our understanding of excitons in monolayer TMDs and contributes to the application of $MoTe_2$ in NIR quantum opto-electronic devices.

Chapter 1

Introduction

A brief description of the experimental and theoretical background is provided. We introduce the topic of monolayer 2H-phase transition metal dichalcogenides (TMDs), $MoTe_2$ in specific, Rydberg excitons in two-dimensional (2D) systems, electroluminescence (EL) in 2D TMDs, the experimental characterization techniques used in this work, and state the research goal of the thesis.

1.1. Monolayer 2H-phase TMDs

Monolayers of transition metal dichalcogenides (TMDs) in the 2H-phase, with chemical formula MX_2 (M = Mo or W, and X = S, Se, or Te), are direct bandgap semiconductors with a two-dimensional (2D) nature and a hexagonal crystal structure[1,2] (Fig. 1). Due to broken inversion symmetry in monolayer TMDs, the different energy-degenerated valleys K^+ and K^-, in momentum space, can couple to circularly polarized light of different chirality. Fig. 2 presents schematically the band structure of a monolayer MX_2 in the single-particle picture, showing the valley selectiveness of optical transitions. The interplay between broken inversion symmetry and spin-orbit coupling (SOC) in TMDs yields a splitting of the lowest conduction bands (Δ_c in Fig. 2) and the highest valence bands.

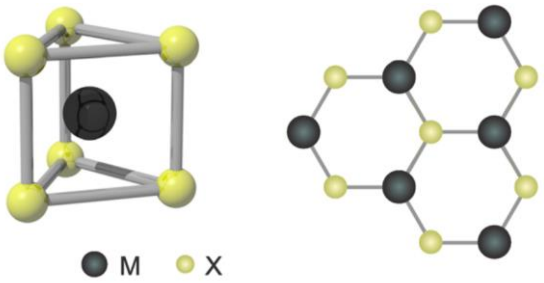

Figure 1. Hexagonal crystal structure of monolayer TMDs. Black (yellow) denotes metal (chalcogen) atoms. Adapted from reference [2].

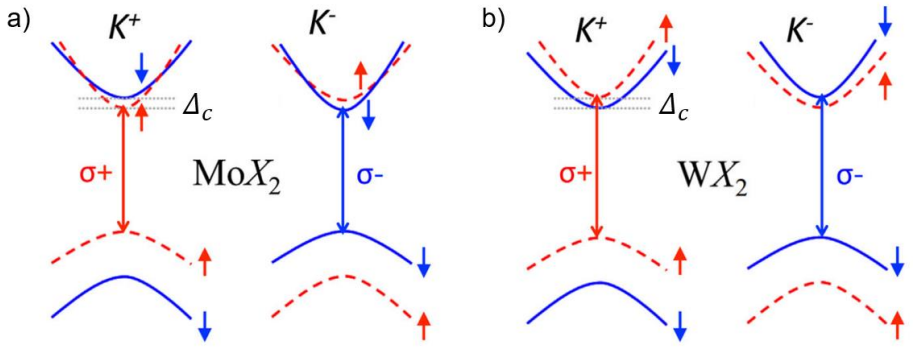

Figure 2. Schematic illustrations of the energy-degenerated valleys K^+ and K^- in momentum space in monolayer TMDs. The order of the conduction bands is opposite in MoX_2 (a) and WX_2 (b), leading to opposite signs for Δ_c in a) and b). Adapted from reference [1].

The optical properties of monolayer TMDs are governed by excitons, which are bound electron-hole pairs. In 2D materials, the dielectric screening of carriers is significantly reduced, leading to enhanced Coulomb interactions.[1,3] Thanks to the enhanced Coulomb interactions, these excitons have large binding energies that result in strong optical resonances.[4–6] To date, much interest has been focused on monolayer TMDs whose electronic bandgap lie in the visible regime of the electromagnetic spectrum such as WS_2, WSe_2, MoS_2 and $MoSe_2$.[7–12]

1.2. $MoTe_2$

$MoTe_2$ has a bandgap in the near-infrared (NIR) regime[13,14] (Fig. 3) very similar to that of silicon (~1.1 eV), which makes it a promising candidate to be used in NIR opto-electronic devices (Fig. 4).[15–17]

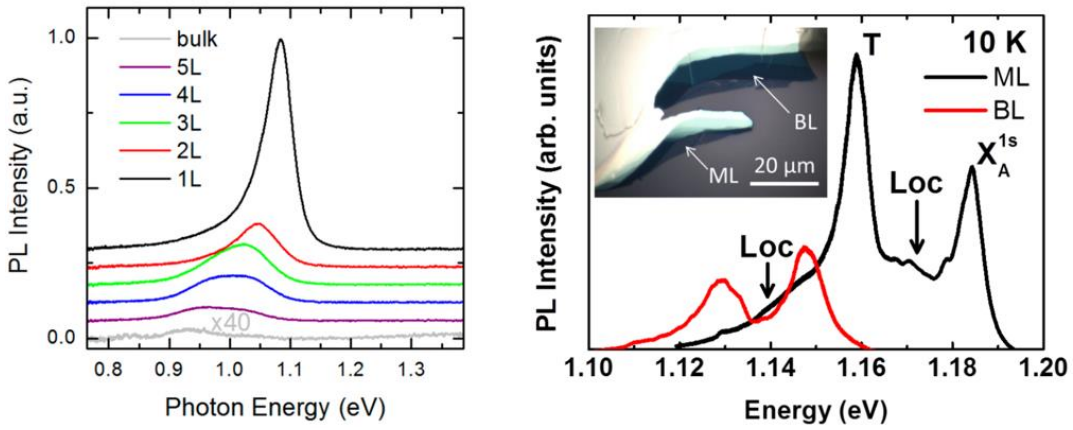

Figure 3. Photoluminescence spectra of $MoTe_2$ samples showing excitonic peaks with energies in the NIR. Adapted from references [13,14].

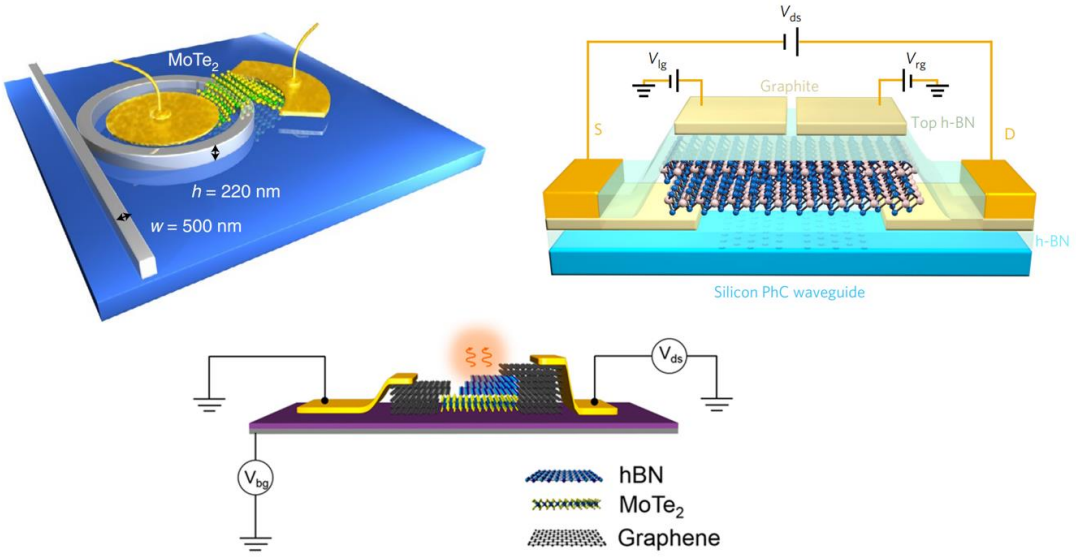

Figure 4. NIR optoelectronic devices with $MoTe_2$ as the active optical component. Adapted from references [15–17].

SOC is particularly high in $MoTe_2$ due to the presence of heavy tellurium atoms.[18] This strong SOC induces a large conduction band splitting and dark-bright energy splitting in $MoTe_2$ (Fig. 5).[14] Bright (dark) excitons refer to the spin allowed (forbidden) transitions between valence and conduction bands in monolayer TMDs. The strong SOC in $MoTe_2$ could facilitate the emergence of chiral topological excitons and polaritons through the application of position-dependent magnetic fields,[19] (Fig. 6a) or through microcavities or surface acoustic waves in combination with a constant magnetic field (Fig. 6b).[20]

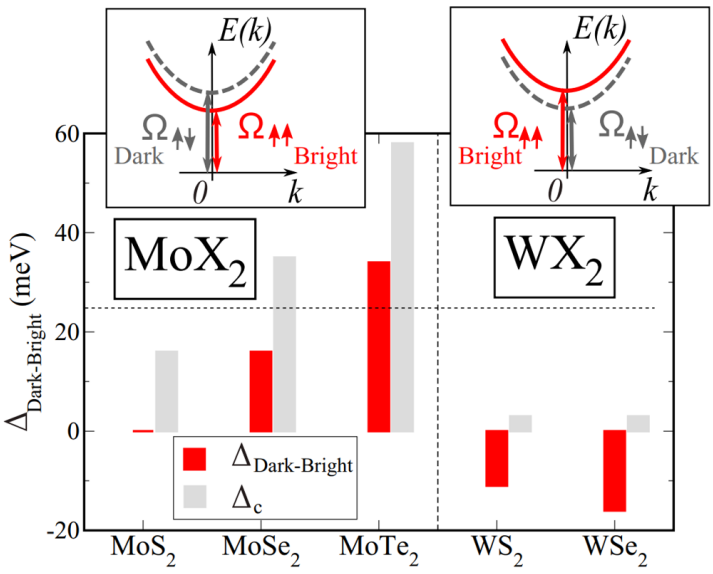

Figure 5. Conduction band energy splitting induced by spin-orbit coupling Δ_c, and dark-bright energy splitting $\Delta_{Dark-Bright}$ of excitons in MoX_2 and WX_2 systems. The bright exciton energy is set to 0. Insets are the corresponding qualitative band structure of the excitons in MoX_2 (left) and WX_2 (right), with bright and dark excitons in red and dotted gray, respectively. Adapted from reference [14].

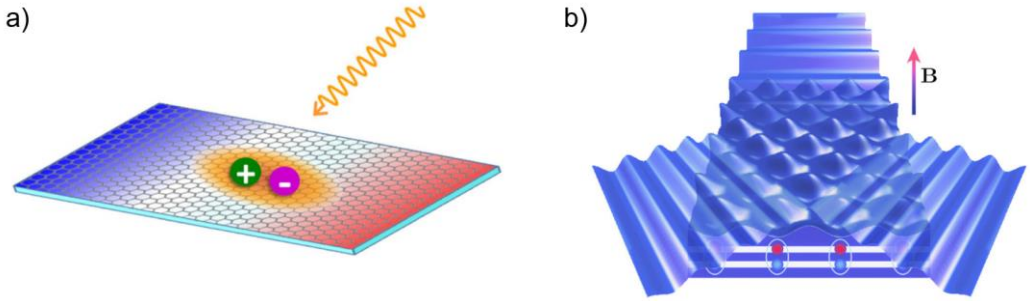

Figure 6. Chiral topological excitons. a) Schematic of generation of topological excitons in the vicinity of a magnetic field domain wall. Adapted from reference [19]. b) Schematic of surface acoustic wave generation of topological polaritons, using a constant magnetic field. Adapted from reference [20].

The bandgap of $MoTe_2$ can be tuned through electrostatic gating[21–23] and tensile strain,[24–28] and its crystal structure may undergo a phase transition from 2H phase to 1T' phase when enough gating or strain is applied (Fig. 7).[21–28]

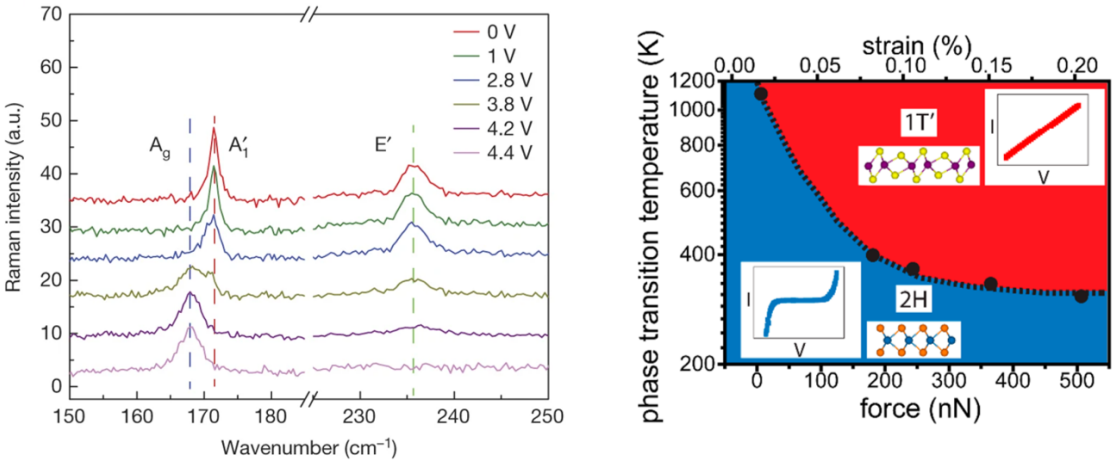

Figure 7. Examples of 2H to 1T' phase transition in $MoTe_2$ through electrostatic gating (left) and tensile strain (right). Adapted from references [22,24].

1.3. Hydrogenic Rydberg series for excitons in 2D systems

In the 2D Rydberg series model for the excitonic quantum states in monolayer TMDs, the exciton emission energies follow the relation[29]

$$E_n = E_g - E_{b(1)}/(2n-1)^2, \qquad (1)$$

where E_g is the free-particle bandgap, $E_{b(1)}$ is the binding energy of the ground state ($n = 1$), and $n = 1,2,3,\ldots$ is the quantum number of the Rydberg energy states (1s, 2s, 3s, …). The binding energy of the Rydberg states reads

$$E_{b(n)} = 2\hbar^2/(\mu r_n^2), \qquad (2)$$

where $\hbar$ is the Planck's constant, μ is the exciton reduced mass, and r_n is the exciton effective Bohr radius. Thus, $E_{b(2)}$ is expected to be nine times smaller than $E_{b(1)}$, making r_2 three times larger than r_1.

Recently, exciton states up to 3s have been observed in photoluminescence (PL) measurements on monolayer $MoTe_2$, using a Salisbury-screen geometry to enhance the PL signal (Fig. 8).[30] This finding makes $MoTe_2$ a good candidate to be used in NIR quantum sensing, given the larger Bohr radii of the excited excitons in the Rydberg

series.[31–33] Fig. 9 shows examples of Rydberg excitons in monolayer TMDs used as quantum sensors, enabling the observation of strongly correlated states in 2D materials.[31,32]

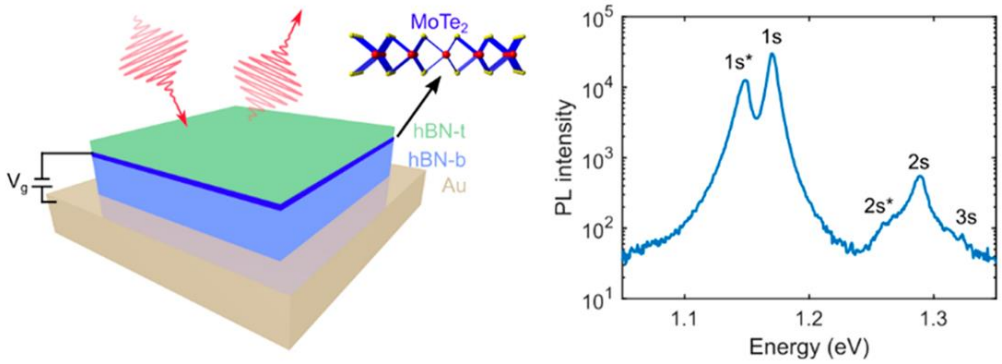

Figure 8. Rydberg excitons in a monolayer $MoTe_2$ heterostructure with Au back reflector for PL enhancement. Adapted from reference [30].

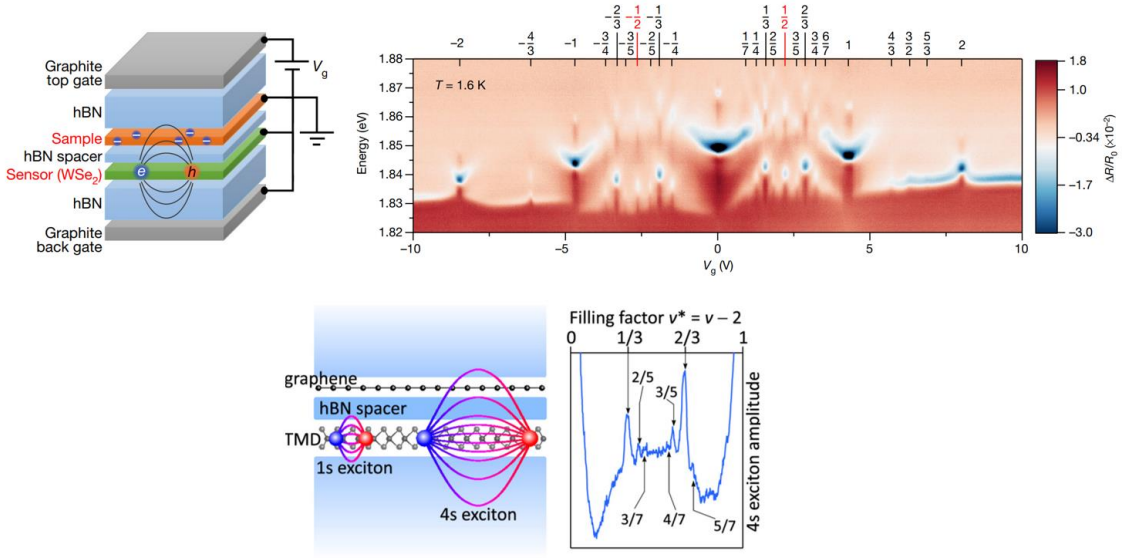

Figure 9. Rydberg excitons in monolayer TMDs functioning as quantum sensors. Top: correlated insulating states in a WSe_2/Ws_2 moiré superlattice observed in the 2s exciton reflectance spectra of monolayer WSe_2. Bottom: fractional quantum Hall states in graphene observed through the 4s exciton amplitude of monolayer $MoSe_2$. Adapted from references [31,32].

1.4. Electroluminescence in 2D TMDs

The electrical generation of excitons[34] or electroluminescence (EL) is an important capability of monolayer TMDs, useful for studying fundamental physics phenomena and opto-electronic device applications. Several methods to generate excitons from electrical

injection include tunneling diodes (Fig. 10a),[35,36] devices using AC voltage between semiconductor and gate (Fig. 10b),[37,38] p-n junctions from split-gate heterostructures (Fig. 10c),[39,40] and the use of metallic contacts or heavily doped silicon to locally form p-n junctions (Fig. 10d).[41–43] Particularly at cryogenic temperatures, it has been shown that electrically generated excitonic emission comes from localized or charged excitons, in addition to neutral excitons,[34,44,39,35,37,38] as shown in Fig. 11.

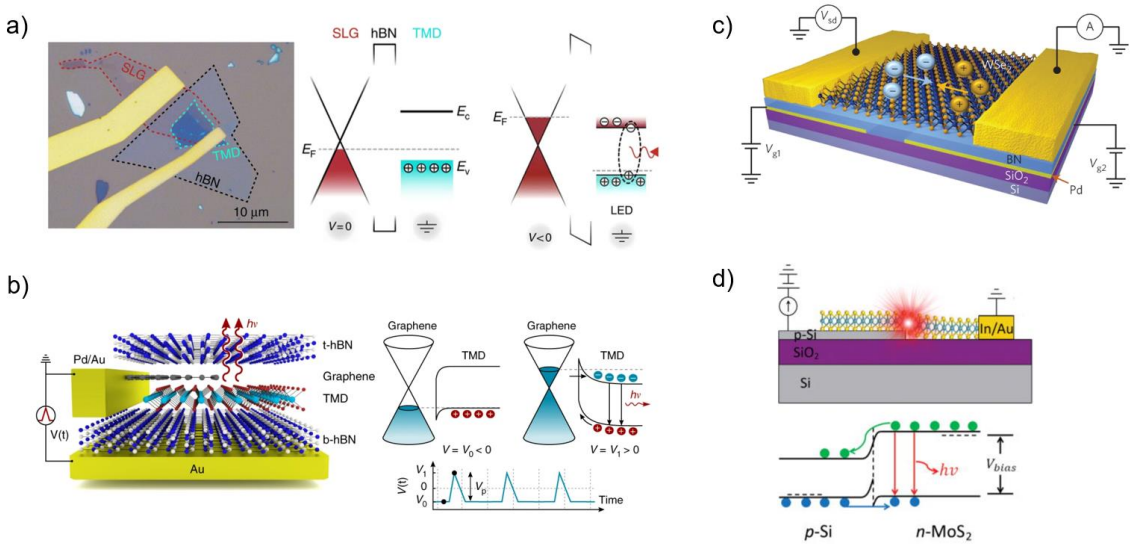

Figure 10. Examples of exciton generation from electrical injection of carriers in 2D TMDs. a) Tunneling of electrons through thin hBN, from graphene to TMD. Adapted from reference [35]. b) A pulsed AC voltage between TMD and gate allows exciton emission. Adapted from reference [38]. c) A split gate heterostructure produces electron- and hole-doped regions in the TMD, forming a p-n junction in between. Adapted from reference [39]. d) Heavily doped silicon and electron doped MoS_2, partially on top of it, form a p-n junction. Adapted from reference [41].

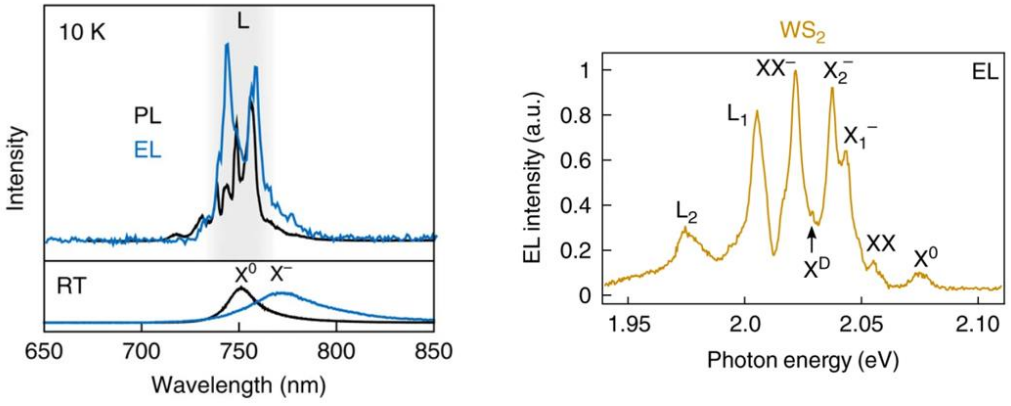

Figure 11. EL from neutral, charged, and localized excitons in 2D TMDs. Adapted from references [35,38].

1.5. Experimental characterization techniques

1.5.1. Raman spectroscopy

Raman spectroscopy is used to determine the vibrational and/or rotational modes of molecules. It relies on inelastic scattering of monochromatic light, and provides important structural information about different materials. A photon excites the material to a virtual energy state momentarily before the photon is scattered with a different, specific energy. This photon energy shift corresponds to the specific vibrational/rotational state, or phonon mode, in the material.

The relative intensities of characteristic Raman peaks can be used for the identification of the numbers of layers in 2D TMDs. When a system goes from 3D to 2D, the translation symmetry along the out-of-plane direction is broken.[45] In few layer $MoTe_2$, this asymmetry activates the mode B_{2g} (Fig. 12), which is optically inactive in the bulk. On the other hand, monolayer $MoTe_2$ is translational symmetric and therefore B_{2g} is absent. The in-plane mode E^1_{2g} achieves its highest intensity for 2L or 3L, as shown in the Raman spectra and spatial maps of Fig. 12.

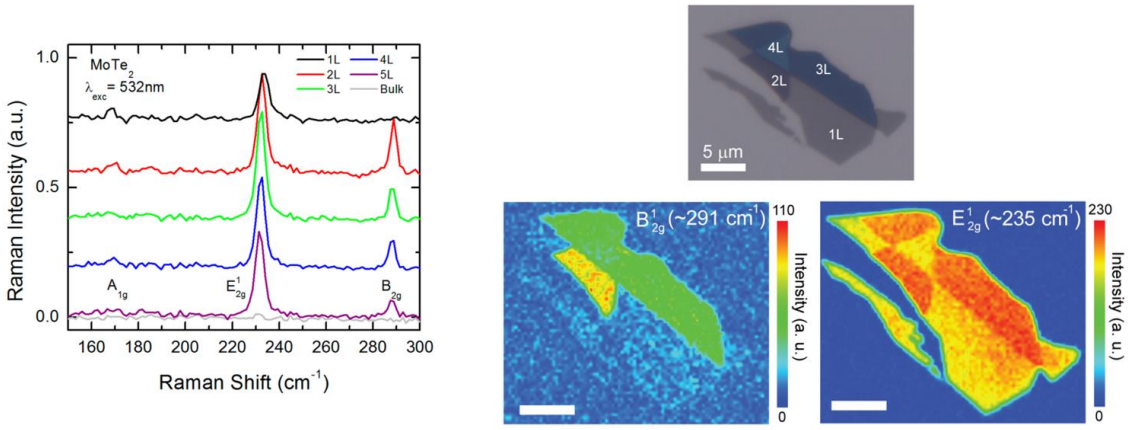

Figure 12. Raman spectra and Raman spatial maps of $MoTe_2$ samples. Absence of B_{2g} peak is evidence of monolayer nature in $MoTe_2$. Adapted from references [13,46].

In the present work, Raman measurements were performed by Marshall Campbell using a Raman setup (Horiba LabRamHR) in a 4 K liquid helium cryostat (Oxford instruments

MicrostatHiRes) at Los Alamos National Laboratory. The sample was illuminated with a 532 nm continuous wave laser and had a spot size of ~1 μm.

1.5.2. Luminescence spectroscopy

Luminescence is the spontaneous emission of light from a material that has been excited into a higher energy state. In a semiconductor, luminescence occurs when an electron that has been excited to the conduction band recombines radiatively with a hole in the valence band. Photoluminescence and electroluminescence are two forms of luminescence used in the study of 2D semiconductors (Fig. 3, Fig. 8, and Fig. 11). In PL, the electrons are excited to the conduction band after the material absorbs photons with energy larger than its bandgap. In EL, electrons and holes recombine as a response to an electric current of electric field through the semiconductor.

PL and EL measurements were performed in a closed-cycle optical cryostat (Montana Instruments s100) under high vacuum (less than 10^{-5} mTorr), integrated into a home-made, scanning, confocal PL setup. This setup includes a 100× magnification (NA = 0.75) objective lens before the sample. A long-pass dichroic mirror at λ = 685 nm followed by a 664 nm long-pass edge filter is used to filter out the incident laser light from the sample emission. For PL measurements, a continuous-wave 658 nm diode laser was directed onto the sample to optically excite a spot size of ~1 μm. For EL measurements, a source-meter (Keithley 2612A) was used to create a voltage difference between electrodes and induce a direct current. This source-meter also controlled the gate voltage. The PL and EL emission were spectrally resolved by a 150 l/mm grating blazed at 800 nm and detected by an air-cooled charge-coupled device (Princeton Instruments SpectraPro HRS-300 spectrometer and PIXIS 1024B CCD).

1.6. Research objective

The main goal of this thesis is the experimental observation of neutral, charged, and excited exciton species in monolayer 2H-$MoTe_2$, by means of PL and EL measurements. Specifically, we aimed at identifying the Rydberg series of excitons (1s and 2s states), and at realizing a NIR LED in BN-encapsulated monolayer $MoTe_2$ heterostructures.

Chapter 2

Fabrication of monolayer $MoTe_2$ devices

In this section, details are presented for single crystal growth, exfoliation, and transfer of $MoTe_2$ samples, nanofabrication of electrodes, and monolayer confirmation for $MoTe_2$.

2.1. $MoTe_2$ single crystal growth

The crystal growth was performed by Dr. Jinyu Liu. Bulk single crystals of 2H-phase $MoTe_2$ were synthesized using the flux method with excess tellurium serving as flux. Molybdenum powder (99.999%, Alfa Aesar, Inc.) was initially arc-melted into a metal pellet, which was then loaded into a quartz tube alongside tellurium chunks (99.999%, Alfa Aesar, Inc.) in a mole ratio of 1:25. Following three cycles of vacuum pumping and argon gas flushing, the quartz tube was sealed under high vacuum conditions. The raw materials were then heated to 1000 °C for 24 hours and slowly cooled to room temperature at a rate of 2 °C per hour (Fig. 13). Subsequently, the resulting mixture was vacuum sealed in a new quartz tube with quartz wool. It was heated to 500 °C, allowed to reach thermal equilibrium, and then subjected to centrifugation to separate the single crystals from the excess flux. Ultimately, hexagonal plate-like single crystal pieces (Fig. 14), measuring up to 3 mm, were obtained. A scanning electron microscopy (SEM) image of one such crystal is shown in Fig. 15, displaying high crystallinity.

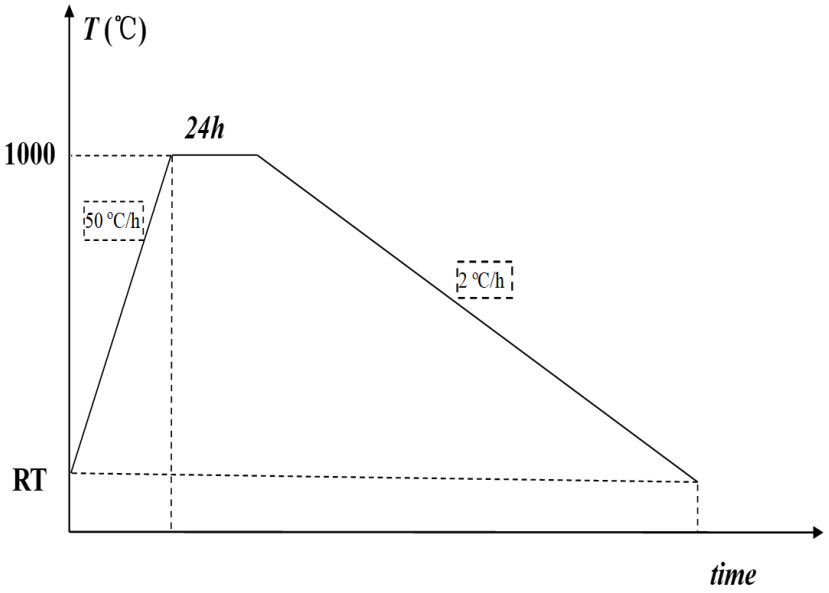

Figure 13. Temperature as a function of time in the process of 2H-$MoTe_2$ crystal growth. RT is room temperature.

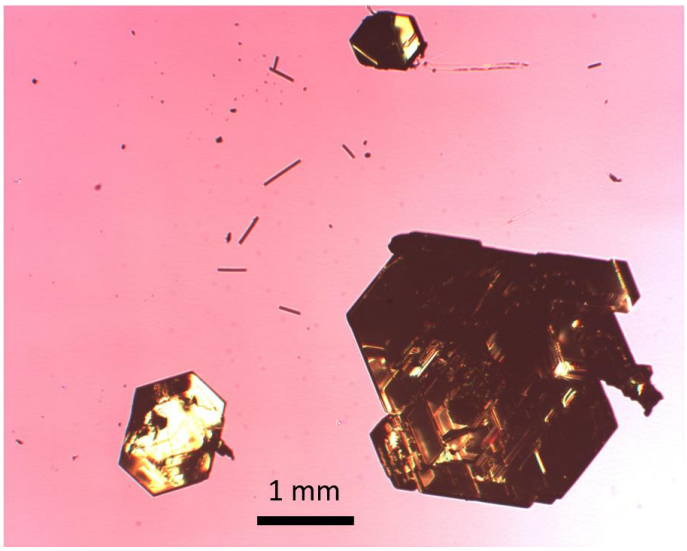

Figure 14. Optical image of bulk 2H-$MoTe_2$ crystals grown by the flux method.

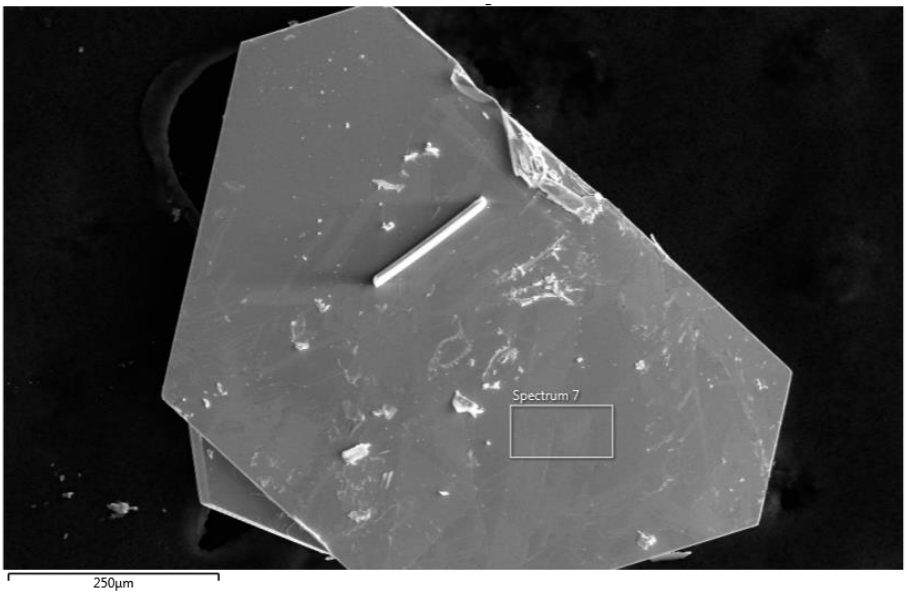

Figure 15. SEM image of 2H-$MoTe_2$ crystal.

2.2. Exfoliation

Bulk $MoTe_2$, BN and graphite were mechanically exfoliated using adhesive tape and transferred onto SiO_2 (285 nm)/Si chips. For $MoTe_2$, the exfoliation was performed inside an argon-filled glove box with concentrations of 0.01 ppm H_2O and 0.33 ppm O_2. In this case, before peeling off the tape, the substrates were heated at 100 °C for ~5 minutes and let cool down to room temperature, so as to maximize the contact area between $MoTe_2$ crystal and SiO_2 substrate[47], as illustrated in Fig. 16. Then the peeling-off was done maintaining a low angle between the tape and substrate, in order to try favoring monolayer yield. Examples of the resulting monolayer $MoTe_2$ flakes are shown in Fig. 17.

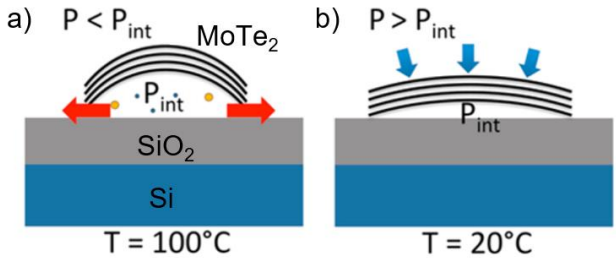

Figure 16. Key part of exfoliation process. a) Heating up the sample to 100 °C allows trapped air between $MoTe_2$ crystal and SiO_2 substrate to exit by pressure difference. b) When the sample is cooled down to room temperature (~20 °C), the pressure difference reverses direction and further reduces the spatial gaps between crystal and substrate. Adapted from reference [47].

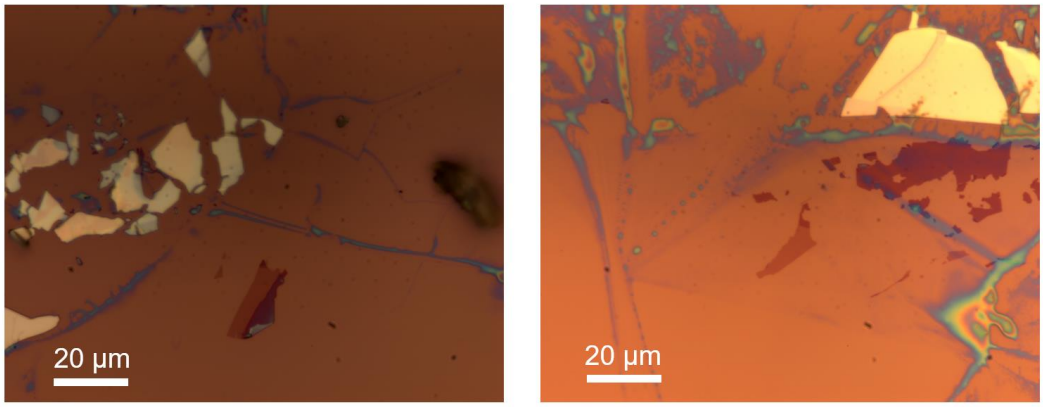

Figure 17. Optical images of exfoliated monolayer $MoTe_2$ flakes.

2.3. Device assembly

A micromanipulator-controlled glass slide, with polydimethylsiloxane (PDMS) and polycarbonate (PC) films attached to it, was used to assemble the BN-encapsulated monolayer $MoTe_2$ heterostructures using a pick-up and drop technique[48] inside the glove box. Fig. 18 presents a series of images that exemplify the device assembly process. First, a BN flake is picked up with a PDMS/PC stamp, and it is subsequently used to pick up a smaller graphite flake (Fig. 18a). The BN/graphite stack is dropped onto a SiO_2/Si chip with previously deposited gold alignment marks, and the remaining PC is dissolved by soaking the chip in chloroform for ~40 minutes (Fig. 18b). Then, a pattern of electrodes is designed and transferred onto the BN flake by electron-beam lithography (EBL), after spin coating a double-layer resist of methyl methacrylate (MMA)/Poly(methyl methacrylate) (PMMA) onto the chip (Fig. 18c). Fig 18d shows the evaporated chromium (Cr, 2 nm)/gold (Au, 10 nm) thin electrodes, after lifting off the excess metal with acetone for ~1 hour. After completing the bottom part of the heterostructure, the top stack was made by picking up another BN and the monolayer $MoTe_2$ sample, and dropping it onto the thin electrodes (Fig. 18e). Finally, EBL-patterned Cr (5 nm)/Au (100 nm) thick electrodes were deposited to contact the thin electrodes and graphite gate (Fig. 18f).

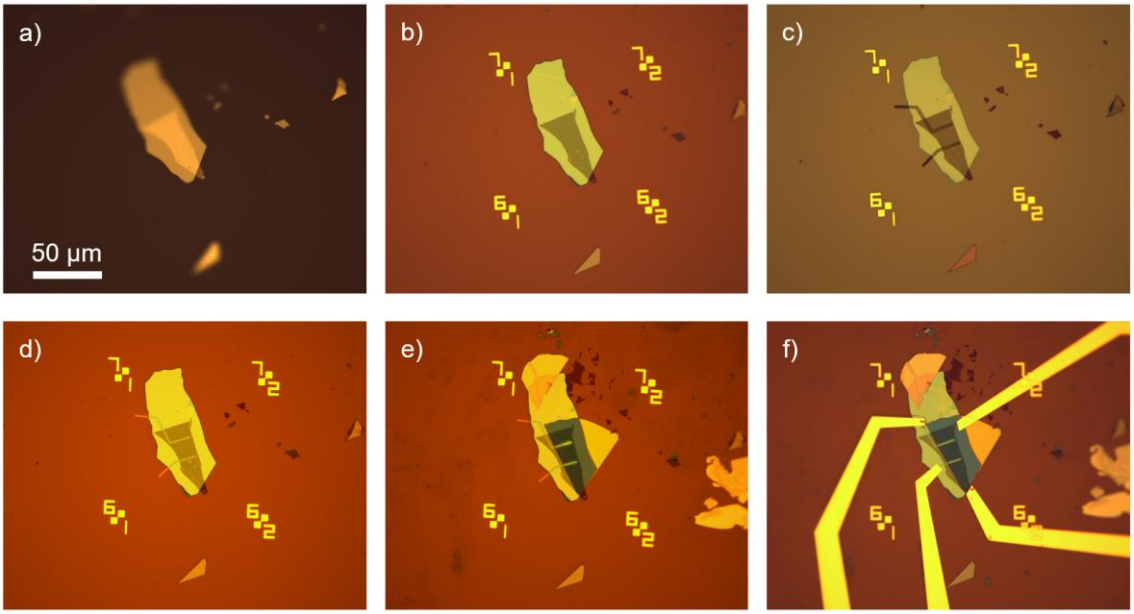

Figure 18. Device assembly process. a) BN and graphite are picked up by the PDMS/PC stamp. b) The BN/graphite stack is transferred onto a SiO_2/Si chip with gold alignment marks. c) EBL pattern of electrodes using MMA/PMMA resist. d) Deposited Cr/Au thin electrodes. e) Pick-up and drop of BN/$MoTe_2$ stack onto the thin electrodes and bottom BN. f) EBL-patterned Cr/Au thick electrodes deposited onto the thin electrodes and graphite gate. Scale bar is the same for all six images.

The fabricated heterostructures are shown schematically in Fig. 19a, b, and Fig 19c, d are optical images of such devices, respectively. Fig 19d is a close-up and upside-down view of Fig. 18f. The 7nm graphite flake at the bottom allows for the application of a gate voltage, V_G, in the $MoTe_2$ sample.

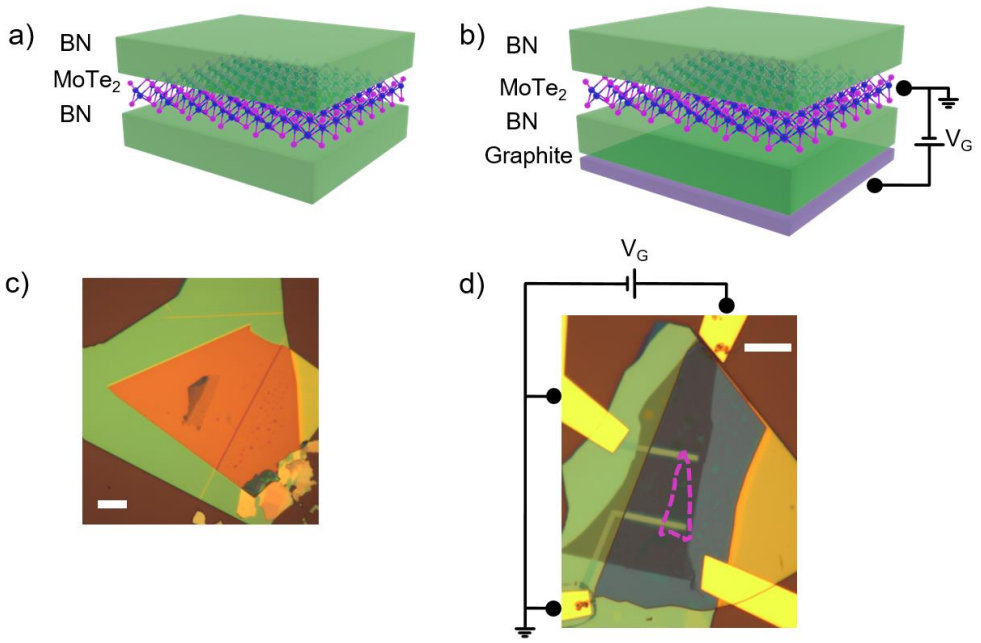

Figure 19. BN-encapsulated monolayer $MoTe_2$ devices. a) and b) Schematics of $MoTe_2$ heterostructures. c) and d) Optical images of $MoTe_2$ heterostructures represented in a) and b), respectively. Scale bars: 10 μm. In b) and d), the electrical connections between electrodes have been drawn for guidance, and V_G is gate voltage. In d), the monolayer sample is outlined in pink.

2.4. Monolayer confirmation

First, the monolayer feature in our $MoTe_2$ exfoliated samples was identified by optical contrast (Fig. 17). Raman measurements were then performed in our $MoTe_2$ samples to further confirm their monolayer identification. Fig. 20 presents the Raman spectra collected at a monolayer region (blue), and a few layer region (red) of the sample in Fig. 19c. The Raman spectra, under illumination with a 532 nm continuous wave laser, reveals distinct features between the monolayer and few layer regions. The absence of the B_{2g} mode and the weaker Raman response of the E^1_{2g} mode in the monolayer region,[13,46] compared to the few-layer region, indicate that our sample is indeed a single layer of $MoTe_2$. The broken translation symmetry of the few layer $MoTe_2$,[45] which activates the out of plane mode B_{2g}, is restored in the monolayer and B_{2g} disappears accordingly.

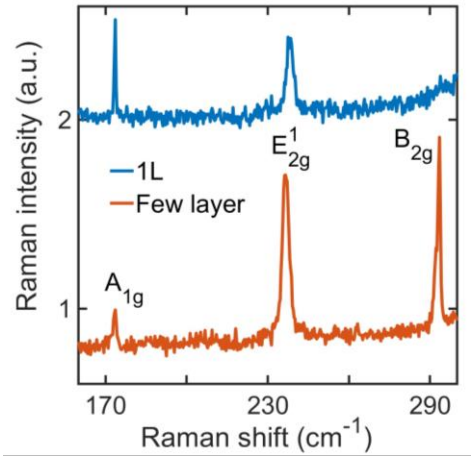

Figure 20. Raman spectrum of monolayer and few-layer regions of the $MoTe_2$ sample. A_{1g}, E^1_{2g} and B_{2g} correspond to different vibrational modes of 2H-phase $MoTe_2$.

Chapter 3

Rydberg excitons in monolayer $MoTe_2$

Here we present the results from the experimental observation of Rydberg exciton states 1s and 2s. Their binding energies are estimated, and their gate voltage dependence and excitation power dependence are acquired through PL measurements. Additionally, we provide details about the etaloning effect in our spectra and the FFT filter designed to minimize it, and the Lorentzian fittings used for the PL and EL spectra in this thesis.

3.1. Binding energies of Rydberg excitons

Fig. 21 is a PL spectrum taken at $T = 4$ K from the BN-encapsulated monolayer $MoTe_2$ device of Fig. 19c. We observed three different peaks with energies in the NIR regime. We attribute these peaks to the ground state neutral exciton, X_{1s}^{0}, the ground state charged exciton, X_{1s}^{T}, and first excited state exciton, X_{2s}^{0}, of the Rydberg series, in accordance with previous reports on $MoTe_2$ monolayers.[30,49] Fig. 21 shows two important features of the 1s state probed by PL: the exciton peak has a narrow linewidth (~4 meV) and the X_{1s}^{T}/X_{1s}^{0} intensity ratio is fairly small (~13 %), both of which are indicative of high sample quality.[30] Moreover, the observation of X_{2s}^{0} without the use of PL enhancement[30] further confirms the high quality of our $MoTe_2$ sample.[49]

Based on the emission energies of X_{1s}^{0} and X_{2s}^{0} (Fig. 21) and equation (1), we estimated the binding energies of the 1s and 2s excitons to be around 151 meV and 17 meV,

respectively, which agrees well with the expected binding energy ratio of $X_{1s}^0/X_{2s}^0 \sim 9$. Following equation (2), these results indicate that the Bohr radius of X_{2s}^0 is about three times larger than that of X_{1s}^0 in our $MoTe_2$ sample. The approximate size of the Rydberg excitons in $MoTe_2$ is illustrated in the inset of Fig. 21, where the 2s exciton corresponds to the large sphere and the 1s exciton to the small sphere. Both 1s and 2s excitons emit NIR light when electrons and holes recombine radiatively. We also estimated the free-particle energy bandgap to be 1.343 eV, which agrees well with the bandgap obtained in another study for BN-encapsulated monolayer $MoTe_2$ through magneto-optical spectroscopy[50] (7% difference from 1.352 eV).

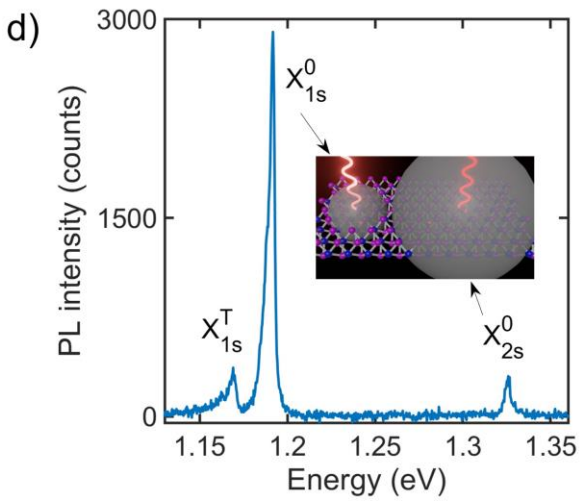

Figure 21. Photoluminescence spectrum of monolayer $MoTe_2$ showing the 1s neutral exciton, X_{1s}^0, 1s charged exciton, X_{1s}^T, and 2s neutral exciton, X_{2s}^0, of the Rydberg series. Inset: Illustration of 1s and 2s excitons, corresponding to smaller and larger Bohr radii, respectively.

3.2. Gate voltage dependence of Rydberg excitons

Rydberg excitons in monolayer TMDs are very sensitive to changes in their electronic landscape.[12,30,51,52] By means of a graphite bottom gate (Fig. 18 and Fig. 19b, d), we applied a gate voltage, V_G, to tune the carrier density of monolayer $MoTe_2$. Fig. 22a, c show colormaps representing the gate voltage dependence of the PL intensity for the 1s and 2s states, respectively. The peak intensity of the 1s neutral exciton indicating the

charge neutrality point (CNP), happens around V_G = -0.1 V. Fig. 22b, d are line cuts of Fig. 22a, c showing that, for both the 1s and 2s states, the PL emission is dominated by neutral excitons when the chemical potential is close to the CNP at V_G = 0 V, and then it becomes dominated by charged excitons when V_G = 1 V and V_G = -1 V, away from CNP. This is the expected behavior of Rydberg excitons in monolayer TMDs upon an increase of the carrier density,[12,30,51,52] since there are more free carriers that prefer to bind to excitons to lower the total energy of the 2D system.[53]

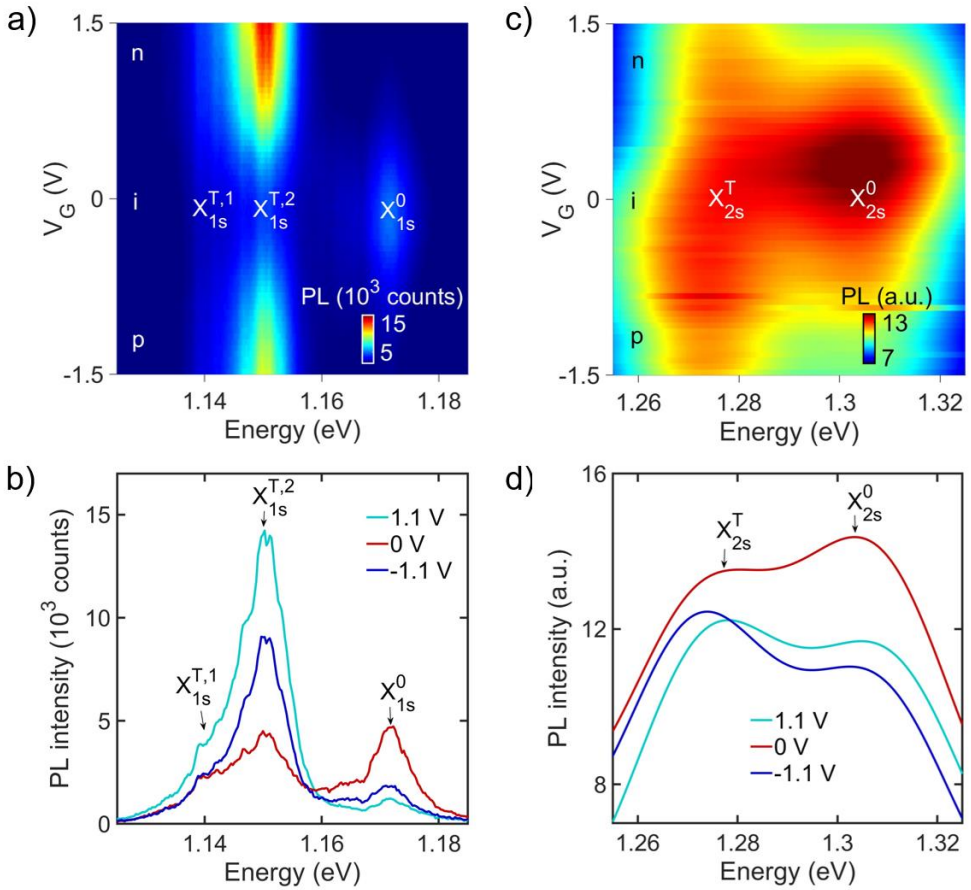

Figure 22. Gate voltage dependence of Rydberg states in monolayer $MoTe_2$. a) PL intensity colormap as a function of energy and V_G for the 1s Rydberg state, showing two charged 1s excitons $X_{1s}^{T,1}$ and $X_{1s}^{T,2}$, and the neutral 1s exciton X_{1s}^{0}. b) Line cuts of (a) at V_G = 1.1 V, 0 V and -1.1 V. c) PL intensity colormap as a function of energy and V_G for the 2s Rydberg state, showing the charged 2s exciton X_{2s}^{T} and the neutral 2s exciton X_{2s}^{0}. d) Line cuts of (c) at V_G = 1.1 V, 0 V and -1.1 V. In (a) and (c) the letters n, i, and p denote electron-doped, intrinsic, and hole-doped regimes, respectively.

We used a Fast Fourier Transform (FFT) filter for the 2s state PL data in Fig. 22c, d, in order to minimize the spectral etaloning interference effect, which is intrinsic to the optical sensor in our PL setup (see Sec. 3.4). Taking a closer look at the energies of neutral and charged excitons of the 1s state (Fig. 22b), we note there are in total three main peaks: two bright charged exciton peaks, $X_{1s}^{T,1}$ at 1.141 eV and $X_{1s}^{T,2}$ at 1.149 eV, arising mainly from SOC splitting of the conduction band,[53] and the neutral exciton peak, X_{1s}^{0}, at 1.172 eV.

3.3. Power dependence of Rydberg excitons

To confirm our identification of the 1s and 2s neutral and charged exciton states in the PL spectra of monolayer $MoTe_2$, we performed power-dependent PL measurements, as shown in Fig. 23a, c. Focusing first on the 1s state, we fitted a sum of four Lorentzian functions to the PL spectra and calculated the integrated PL intensity of the four excitonic species as power increases (Fig. 23b). Included in Fig. 23b are power-law fittings to the integrated PL intensity of the form $I_{PL} = CP^{\kappa\alpha}$, where C and κ are dimensionless constants, P is the laser power, and α is a coefficient indicating the nature of the excitonic species. We calculated $\kappa = 0.67$ by setting $\alpha \equiv 1$ for the neutral exciton X_{1s}^{0} and used this as a reference to extract the α coefficients for the other excitonic species.[38] We used the constant κ in the power-law fittings to account for the nonlinear increase of X_{1s}^{0} intensity with power, which is likely a result of loss of exciton population to a defect-related localized state[54] near X_{1s}^{0} (Sec. 3.5). In this scenario, both charged excitons $X_{1s}^{T,1}$ and $X_{1s}^{T,2}$ increase superlinearly with power ($\alpha = 1.35$ for $X_{1s}^{T,1}$ and $\alpha = 1.28$ for $X_{1s}^{T,2}$), in accordance with previous studies.[38,55,56]

In the case of 2s state excitations, we fitted a sum of two Lorentzian functions to the PL spectra accounting for the 2s state neutral exciton X_{2s}^{0} and charged exciton X_{2s}^{T}. Fig. 23d

shows the increase rate of the integrated PL intensity for X_{2s}^{0} and X_{2s}^{T} with power. From power-law fittings, again setting $\alpha \equiv 1$ for X_{2s}^{0}, we note that X_{2s}^{T} increases sublinearly ($\alpha = 0.88$) with power rather than superlinearly like $X_{1s}^{T,1}$ and $X_{1s}^{T,2}$ do. This trend may be related to the larger linewidths of 2s exciton species (~40 meV) compared to those of 1s exciton species (~12 meV). The large linewidths of the 2s excitations could have prevented us from resolving peaks associated with localized states energetically near X_{2s}^{0} and X_{2s}^{T}. Loss of exciton population to localized states[54] would then affect the increase of X_{2s}^{T} intensity with power.

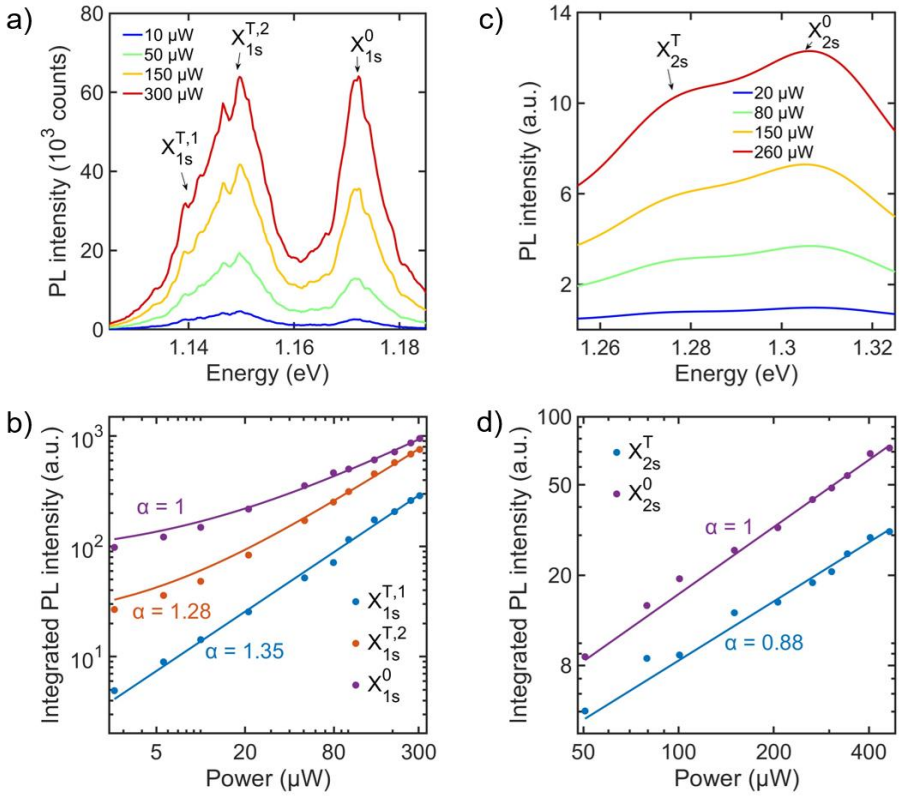

Figure 23. Laser power dependence of Rydberg states. a) and c) PL spectra at different laser power for the 1s and 2s states, respectively. b) and d) Integrated PL intensity as a function of power extracted from Lorentzian fittings to the power-dependent PL spectra for the 1s and 2s states, respectively. The solid lines are power law fittings of the integrated PL intensity dependence on power. The coefficients α are extracted from these fittings and indicate the nature of the excitonic species.

3.4. Etaloning effect and FFT filtering

Our spectrometer uses a standard back-illuminated silicon-based CCD camera (PIXIS 1024B). In this device, the discontinuity in the refractive indices of the top and bottom layers produces reflection back into the CCD. At NIR wavelengths, light can bounce back and forth through the CCD and form a resonant optical cavity, effectively acting as an etalon. This etalon behavior produces an unavoidable set of fringes of constructive and destructive interference that artificially modifies the spectrum one measures. The typical thickness of the silicon layer (around 10 to 15 μm) determines the typical periodicity of the interference pattern to be around 5 nm. This wavelength period translates to a ~5 meV periodicity in energy and distorts our PL spectra. In our measurements, the etaloning affected more the 2s state excitons than the 1s excitons. We suggest this happened because of the rather smaller number of PL counts in the 2s state (2s/1s PL intensity ratio is ~16 %), and its large linewidths (three times larger than that of 1s state).

In order to minimize the etaloning effect on the 2s state excitons of the PL spectra, we applied a Fast Fourier Transform (FFT) filter after slightly modifying an open-source MATLAB code, made by Shmuel Ben-Ezra in 2009. We attempted to remove frequencies corresponding to the CCD etalon periodicity of about 5 to 10 meV. The FFT filter performs the Fourier transform of the 2s state PL intensity, filters out frequencies larger than 25 Hz, and reconstructs the signal in the energy domain. The resulting filtered 2s PL spectra is shown in Fig. 22c, d and Fig. 23c.

3.5. Lorentzian fittings and localized exciton state

Lorentzian functions of the form $I_i = \frac{A_i}{1+\left(\frac{E-E_i}{\Gamma_i/2}\right)^2}$ were fitted to the PL and EL intensity spectra to extract the integrated intensity of each excitonic species. A_i is the amplitude,

E_i is the emission energy of the excitonic species, and Γ_i is the linewidth (full width at half-maximum). The fittings were performed in MATLAB using a slightly modified version of an open-source code made by Erik Bauch in 2017. A total of four Lorentzian profiles were used to fit the PL/EL data to include contributions from the neutral exciton, two charged excitons, and an additional small peak in between neutral and charged excitons, which is attributed to a localized state.[14] From the fittings, the energy of this additional peak is around 1.162 eV, and its identification as a localized state is confirmed by the sublinear[57–60] increase of its intensity with power in PL and EL (Sec. 4.2).

Chapter 4

Electroluminescence from p-n junctions in monolayer $MoTe_2$

This chapter reports on the excitonic EL observed in our $MoTe_2$ device, the I-V measurements indicating diode behavior, and provides an explanation for the p-n junctions formed in the sample near the electrodes.

4.1. Electrically generated neutral and charged excitons

By placing monolayer $MoTe_2$ on top of two gold electrodes (Fig. 18e, Fig. 19d, and Fig. 24a) in an inert environment, therefore keeping a clean TMD/metal interface, we realized p-n junctions near the electrodes. This was done by (1) locally hole-doping the sample on top of the electrodes[43] and (2) electron-doping the rest of the sample using the graphite bottom gate. In order to perform EL measurements on our monolayer $MoTe_2$, we applied a bias (drain-source) voltage, V_{DS}, between the two gold electrodes underneath each end of the sample to create an in-plane electric field so electrical current can flow through. Fig. 24a shows a spatial map of the integrated EL intensity after applying a gate voltage V_G = 12 V and bias voltage V_{DS} = 30 V by grounding electrode 1 and applying -30 V to electrode 2. Notably, the EL signal comes mainly from the regions of the sample on top of and surrounding both electrodes. Fig. 24b presents an EL spectrum (red curve) collected at a spot of the sample near electrode 2 applying V_G = 10 V and V_{DS} = 30 V,

and compares it to the PL spectrum (blue curve) collected at a spot near the middle of the sample using $V_G = V_{DS} = 0$ V. We identified in this EL spectrum the same three peaks that we observed in the PL spectra, namely, the 1s low energy charged exciton $X_{1s}^{T,1}$ at 1.140 eV, the 1s high energy charged exciton $X_{1s}^{T,2}$ at 1.153 eV, and the 1s neutral exciton X_{1s}^{0} at 1.172 eV.

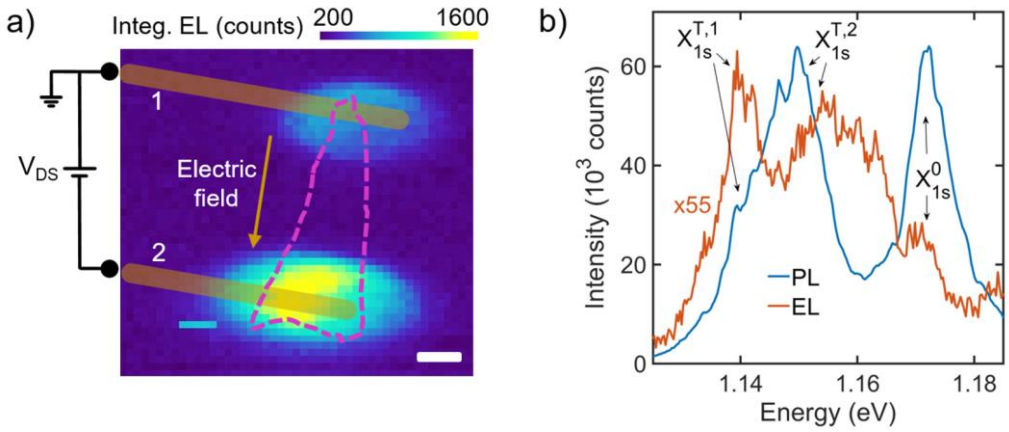

Figure 24. Electroluminescence in monolayer $MoTe_2$. a) Spatial map of the integrated EL intensity of monolayer $MoTe_2$ using $V_G = 12$ V and $V_{DS} = 30$ V. The sample is outlined in pink. Electrode 1 is grounded and electrode 2 is at -30 V. Scale bar: 4 µm. b) PL spectrum (blue) collected at the center of the sample using an incident power of 300 µW, and EL spectrum (red) collected near electrode 2 in the sample using $V_G = 10$ V and $V_{DS} = 30$ V (counts are multiplied by a factor of 55 for the EL spectrum). The neutral exciton X_{1s}^{0} and charged excitons $X_{1s}^{T,1}$ and $X_{1s}^{T,2}$ are identified in both spectra.

In order to understand how the excitonic EL signal is generated, we recorded I_{DS}-V_{DS} curves at various gate voltages and observed the characteristic behavior of a diode, as shown in Fig. 25a. After V_{DS} has reached a certain threshold voltage, the monolayer $MoTe_2$ sample allows a current of electrons to flow from electrode 2 to electrode 1 (Fig. 16a). As V_{DS} is increased further, the sample enters the "linear regime" of the diode where I_{DS} is approximately linear with V_{DS}. In this regime, we estimate the resistance of the monolayer $MoTe_2$ sample to be around ~170 kΩ , including the contact resistance at the two sample/electrode interfaces with $V_G = 12$ V and $V_{DS} = 30$ V. Fig. 25a also shows that the threshold voltage required to initiate the diode decreases as V_G increases. This is because the device needs a smaller electric field to produce a current when more carriers

are present in the sample, thus confirming the diode behavior of our monolayer $MoTe_2$ device.

Fig. 25b schematically shows how the excitonic emission is generated through the p-n junctions that are formed near the electrodes. First, the clean sample/electrode interface allows the gold electrode to locally hole-dope (p) the sample directly on top of it,[43] since the work function of gold (5.31 eV)[61] lies below the valence band maximum of monolayer $MoTe_2$ (5.04 eV).[62] Then, by applying the gate voltage V_G, the rest of the sample is electron-doped (n), and p-n junctions in monolayer $MoTe_2$ are created around each electrode. When the bias voltage V_{DS} is applied in a forward configuration and reaches a certain threshold, the energy barrier between n and p regions of the sample starts to get reduced. In other words, the resistance to flow between these regions becomes finite. Hence, the diode is in the "on" state, as opposed to the "off" state when $I_{DS}/V_{DS} = 1/R = 0$, and the resistance R is infinite. Electrons then start to flow towards the p region and holes flow towards the n region, making it possible for pairs of electrons and holes to bind in the depletion region (on top of and surrounding the electrodes) to form excitons. These excitons can then recombine radiatively and produce the EL spectrum observed (Fig. 24b). In this way, we realized a monolayer $MoTe_2$ NIR light-emitting diode (LED).

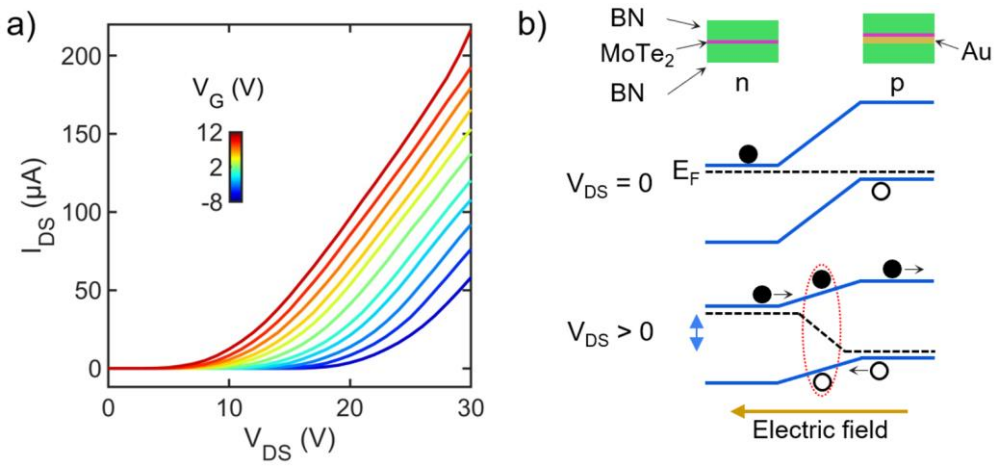

Figure 25. a) I_{DS}-V_{DS} curves of monolayer $MoTe_2$ device. V_G varies from -8 V to 12 V in steps of 2 V. b) Schematic representation of excitonic emission from p-n junctions around electrodes. Top: the n region is formed in the sample far from the electrode, and the p region is formed in the sample on top of the electrode. Middle and bottom: electronic band schematics in the interface between n and p regions (depletion region) leading to excitonic emission when $V_{DS} > 0$.

4.2. Power dependence of EL spectra

To further characterize our monolayer $MoTe_2$ NIR LED, we probed its EL response under different gate voltage V_G. At constant V_{DS}, the electrical current I_{DS} is proportional to V_G and the electrical power that the current carries through the sample, $P = I_{DS}V_{DS}$, is therefore V_G dependent. Thus, the V_G dependence of EL intensity can be thought of as a dependence on power, at constant V_{DS}, which is shown in Fig. 26a for V_{DS} = 30 V. We fitted exponential functions of the form $I_{EL} = Ce^{(\kappa\alpha P)}$ to the integrated EL intensity, where C and κ are dimensionless constants, α is a coefficient that indicates the nature of the excitonic species (just as in the PL measurements), and P is power. Following the same procedure used in a previous EL study on monolayer TMDs,[38] the coefficient of X_{1s}^{0} is fixed to be $\alpha \equiv 1$ and it is used as reference to obtain the α coefficients for the other excitations. Fig. 26b shows that the charged exciton $X_{1s}^{T,1}$ increases superlinearly[38,55,56] with power ($\alpha = 1.25$), just as it was determined in our power-dependent PL measurements (Fig. 23b), whereas $X_{1s}^{T,2}$ increases sublinearly with power ($\alpha = 0.89$). This sublinear trend of $X_{1s}^{T,2}$ as opposed to its superlinear trend found by PL, may be explained by the close proximity to the defect-related localized state around 1.162 eV (from Lorentzian fittings, Sec. 3.5), which would induce loss of exciton population from $X_{1s}^{T,2}$ to this state.[54] Furthermore, the localized state was found to have a larger α coefficient in EL ($\alpha = 0.82$) than in PL ($\alpha = 0.56$). This suggests that, when performing EL measurements, $X_{1s}^{T,2}$ loses enough intensity to the localized state that its intensity increases at a lower rate (sublinear) than in the case of PL measurements (superlinear).

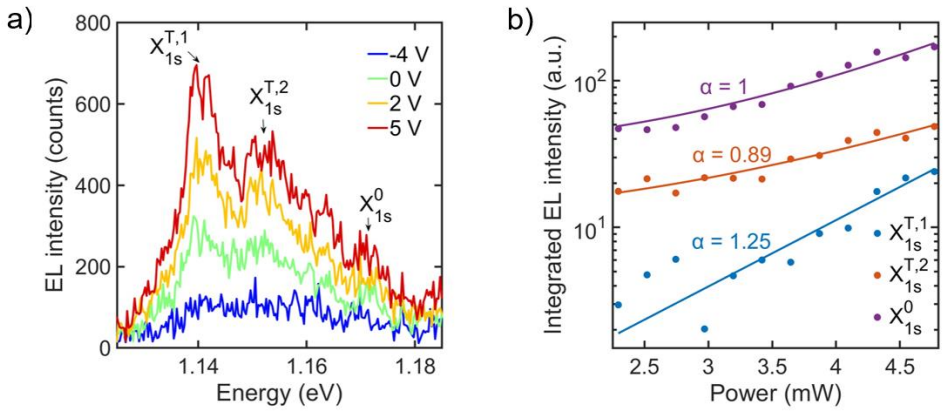

Figure 26. Electrical power dependence of excitonic species in monolayer $MoTe_2$ a) V_G dependence of EL intensity at V_{DS} = 30 V. V_G varies from -4 V to 5 V. b) Integrated EL intensity of $X_{1s}^{T,1}$, $X_{1s}^{T,2}$ and X_{1s}^{0} as a function of electrical power (which is proportional to V_G at constant V_{DS}) extracted from Lorentzian fittings to the power dependent EL spectra. The solid lines are exponential fittings of the EL intensity dependence on power. The α coefficients are extracted from these exponential fittings and indicate the nature of the various excitonic species.

Chapter 5

Conclusion

We report the experimental observation of neutral, charged, and excited exciton species in monolayer 2H-$MoTe_2$, probed by both photoluminescence and electroluminescence measurements at low temperature (T = 4 K). The extremely high quality of our $MoTe_2$ samples allows us to identify the observed optical resonances as the Rydberg series of excitons (1s and 2s states). We also realized a NIR LED in monolayer $MoTe_2$, and were able to resolve the fine structure of the charged ground exciton state, using a simple device geometry. Our observation and analysis of the various excitonic species revealed by both PL and EL in monolayer $MoTe_2$ can lay the foundations to create novel quantum devices based on 2D semiconductors with a bandgap similar to that of silicon, where the role of strong SOC can be enhanced and facilitate the creation of topological opto-electronic devices.

References

1. Wang, G. *et al. Colloquium* : Excitons in atomically thin transition metal dichalcogenides. *Rev. Mod. Phys.* **90**, 021001 (2018).
2. Kiemle, J., Zimmermann, P., Holleitner, A. W. & Kastl, C. Light-field and spin-orbit-driven currents in van der Waals materials. *Nanophotonics* **9**, 2693–2708 (2020).
3. Raja, A. *et al.* Coulomb engineering of the bandgap and excitons in two-dimensional materials. *Nat Commun* **8**, 15251 (2017).
4. Ugeda, M. M. *et al.* Giant bandgap renormalization and excitonic effects in a monolayer transition metal dichalcogenide semiconductor. *Nature Mater* **13**, 1091–1095 (2014).
5. Chernikov, A. *et al.* Exciton Binding Energy and Nonhydrogenic Rydberg Series in Monolayer WS 2. *Phys. Rev. Lett.* **113**, 076802 (2014).
6. Gupta, G., Kallatt, S. & Majumdar, K. Direct observation of giant binding energy modulation of exciton complexes in monolayer MoS e 2. *Phys. Rev. B* **96**, 081403 (2017).
7. Zhu, B., Chen, X. & Cui, X. Exciton Binding Energy of Monolayer WS2. *Sci Rep* **5**, 9218 (2015).
8. Kesarwani, R. *et al.* Control of trion-to-exciton conversion in monolayer WS_2 by orbital angular momentum of light. *Sci. Adv.* **8**, eabm0100 (2022).
9. Huang, J., Hoang, T. B. & Mikkelsen, M. H. Probing the origin of excitonic states in monolayer WSe2. *Sci Rep* **6**, 22414 (2016).
10. Simbulan, K. B. *et al.* Selective Photoexcitation of Finite-Momentum Excitons in Monolayer MoS_2 by Twisted Light. *ACS Nano* **15**, 3481–3489 (2021).
11. Vaquero, D. *et al.* Excitons, trions and Rydberg states in monolayer MoS2 revealed by low-temperature photocurrent spectroscopy. *Commun Phys* **3**, 194 (2020).
12. Liu, E. *et al.* Exciton-polaron Rydberg states in monolayer MoSe2 and WSe2. *Nat Commun* **12**, 6131 (2021).

13. Ruppert, C., Aslan, B. & Heinz, T. F. Optical Properties and Band Gap of Single- and Few-Layer MoTe $_2$ Crystals. *Nano Lett.* **14**, 6231–6236 (2014).
14. Robert, C. *et al.* Excitonic properties of semiconducting monolayer and bilayer MoT e 2. *Phys. Rev. B* **94**, 155425 (2016).
15. Zhu, Y. *et al.* High-Efficiency Monolayer Molybdenum Ditelluride Light-Emitting Diode and Photodetector. *ACS Appl. Mater. Interfaces* **10**, 43291–43298 (2018).
16. Bie, Y.-Q. *et al.* A MoTe2-based light-emitting diode and photodetector for silicon photonic integrated circuits. *Nature Nanotech* **12**, 1124–1129 (2017).
17. Maiti, R. *et al.* Strain-engineered high-responsivity MoTe2 photodetector for silicon photonic integrated circuits. *Nat. Photonics* **14**, 578–584 (2020).
18. Champagne, A. *et al.* Quasiparticle and Optical Properties of Carrier-Doped Monolayer MoTe $_2$ from First Principles. *Nano Lett.* **23**, 4274–4281 (2023).
19. Gong, Z. R., Luo, W. Z., Jiang, Z. F. & Fu, H. C. Chiral topological excitons in the monolayer transition metal dichalcogenides. *Sci Rep* **7**, 42390 (2017).
20. Bardyn, C.-E., Karzig, T., Refael, G. & Liew, T. C. H. Topological polaritons and excitons in garden-variety systems. *Phys. Rev. B* **91**, 161413 (2015).
21. Duerloo, K.-A. N., Li, Y. & Reed, E. J. Structural phase transitions in two-dimensional Mo- and W-dichalcogenide monolayers. *Nat Commun* **5**, 4214 (2014).
22. Wang, Y. *et al.* Structural phase transition in monolayer MoTe2 driven by electrostatic doping. *Nature* **550**, 487–491 (2017).
23. Krishnamoorthy, A. *et al.* Semiconductor–metal structural phase transformation in MoTe $_2$ monolayers by electronic excitation. *Nanoscale* **10**, 2742–2747 (2018).
24. Song, S. *et al.* Room Temperature Semiconductor–Metal Transition of MoTe $_2$ Thin Films Engineered by Strain. *Nano Lett.* **16**, 188–193 (2016).

25. Huang, H. H. *et al.* Controlling phase transition for single-layer MTe_2 (M = Mo and W): modulation of the potential barrier under strain. *Phys. Chem. Chem. Phys.* **18**, 4086–4094 (2016).
26. Hou, W. *et al.* Strain-based room-temperature non-volatile MoTe2 ferroelectric phase change transistor. *Nat. Nanotechnol.* **14**, 668–673 (2019).
27. Deng, Y. *et al.* $MoTe_2$: Semiconductor or Semimetal? *ACS Nano* **15**, 12465–12474 (2021).
28. Ramzan, M. S. & Cocchi, C. Strained Monolayer MoTe2 as a Photon Absorber in the Telecom Range. *Nanomaterials* **13**, 2740 (2023).
29. Trushin, M. Tightly bound excitons in two-dimensional semiconductors with a flat valence band. *Phys. Rev. B* **99**, 205307 (2019).
30. Biswas, S. *et al.* Rydberg Excitons and Trions in Monolayer $MoTe_2$. *ACS Nano* **17**, 7685–7694 (2023).
31. Xu, Y. *et al.* Correlated insulating states at fractional fillings of moiré superlattices. *Nature* **587**, 214–218 (2020).
32. Popert, A. *et al.* Optical Sensing of Fractional Quantum Hall Effect in Graphene. *Nano Lett.* **22**, 7363–7369 (2022).
33. Kazimierczuk, T., Fröhlich, D., Scheel, S., Stolz, H. & Bayer, M. Giant Rydberg Excitons in Cuprous Oxide.
34. Wang, J., Verzhbitskiy, I. & Eda, G. Electroluminescent Devices Based on 2D Semiconducting Transition Metal Dichalcogenides. *Advanced Materials* **30**, 1802687 (2018).
35. Palacios-Berraquero, C. *et al.* Atomically thin quantum light-emitting diodes. *Nat Commun* **7**, 12978 (2016).
36. Liu, C.-H. *et al.* Nanocavity Integrated van der Waals Heterostructure Light-Emitting Tunneling Diode. *Nano Lett.* **17**, 200–205 (2017).

37. Lien, D.-H. *et al.* Large-area and bright pulsed electroluminescence in monolayer semiconductors. *Nat Commun* **9**, 1229 (2018).
38. Paur, M. *et al.* Electroluminescence from multi-particle exciton complexes in transition metal dichalcogenide semiconductors. *Nat Commun* **10**, 1709 (2019).
39. Ross, J. S. *et al.* Electrically tunable excitonic light-emitting diodes based on monolayer WSe2 p–n junctions. *Nature Nanotech* **9**, 268–272 (2014).
40. Baugher, B. W. H., Churchill, H. O. H., Yang, Y. & Jarillo-Herrero, P. Optoelectronic devices based on electrically tunable p–n diodes in a monolayer dichalcogenide. *Nature Nanotech* **9**, 262–267 (2014).
41. Ye, Y. *et al.* Exciton-dominant electroluminescence from a diode of monolayer MoS2. *Applied Physics Letters* **104**, 193508 (2014).
42. Lopez-Sanchez, O. *et al.* Light Generation and Harvesting in a van der Waals Heterostructure. *ACS Nano* **8**, 3042–3048 (2014).
43. Ngo, T. D. *et al.* Fermi-Level Pinning Free High-Performance 2D CMOS Inverter Fabricated with Van Der Waals Bottom Contacts. *Advanced Electronic Materials* **7**, 2001212 (2021).
44. Zhang, Y. J., Oka, T., Suzuki, R., Ye, J. T. & Iwasa, Y. Electrically Switchable Chiral Light-Emitting Transistor. *Science* **344**, 725–728 (2014).
45. Luo, X. *et al.* Effects of lower symmetry and dimensionality on Raman spectra in two-dimensional WSe 2. *Phys. Rev. B* **88**, 195313 (2013).
46. Yamamoto, M. *et al.* Strong Enhancement of Raman Scattering from a Bulk-Inactive Vibrational Mode in Few-Layer MoTe $_2$. *ACS Nano* **8**, 3895–3903 (2014).
47. Huang, Y. *et al.* Reliable Exfoliation of Large-Area High-Quality Flakes of Graphene and Other Two-Dimensional Materials. *ACS Nano* **9**, 10612–10620 (2015).
48. Pizzocchero, F. *et al.* The hot pick-up technique for batch assembly of van der Waals heterostructures. *Nat Commun* **7**, 11894 (2016).

49. Han, B. *et al.* Exciton States in Monolayer MoSe 2 and MoTe 2 Probed by Upconversion Spectroscopy. *Phys. Rev. X* **8**, 031073 (2018).
50. Goryca, M. *et al.* Revealing exciton masses and dielectric properties of monolayer semiconductors with high magnetic fields. *Nat Commun* **10**, 4172 (2019).
51. Wagner, K. *et al.* Autoionization and Dressing of Excited Excitons by Free Carriers in Monolayer WSe 2. *Phys. Rev. Lett.* **125**, 267401 (2020).
52. Goldstein, T. *et al.* Ground and excited state exciton polarons in monolayer MoSe2. *The Journal of Chemical Physics* **153**, 071101 (2020).
53. Yu, H., Cui, X., Xu, X. & Yao, W. Valley excitons in two-dimensional semiconductors. *National Science Review* **2**, 57–70 (2015).
54. You, Y. *et al.* Observation of biexcitons in monolayer WSe2. *Nature Phys* **11**, 477–481 (2015).
55. He, Z. *et al.* Biexciton Formation in Bilayer Tungsten Disulfide. *ACS Nano* **10**, 2176–2183 (2016).
56. Bellus, M. Z., Ceballos, F., Chiu, H.-Y. & Zhao, H. Tightly Bound Trions in Transition Metal Dichalcogenide Heterostructures. *ACS Nano* **9**, 6459–6464 (2015).
57. He, Y.-M. *et al.* Single quantum emitters in monolayer semiconductors. *Nature Nanotech* **10**, 497–502 (2015).
58. Koperski, M. *et al.* Single photon emitters in exfoliated WSe2 structures. *Nature Nanotech* **10**, 503–506 (2015).
59. Srivastava, A. *et al.* Optically active quantum dots in monolayer WSe2. *Nature Nanotech* **10**, 491–496 (2015).
60. Tongay, S. *et al.* Defects activated photoluminescence in two-dimensional semiconductors: interplay between bound, charged and free excitons. *Sci Rep* **3**, 2657 (2013).
61. Lide, D. R. *CRC Handbook of Chemistry and Physics*. (CRC Press, Boca Raton, FL, 2001).

62. Rasmussen, F. A. & Thygesen, K. S. Computational 2D Materials Database: Electronic Structure of Transition-Metal Dichalcogenides and Oxides. *J. Phys. Chem. C* **119**, 13169–13183 (2015).